Aero-Optical Effects of Turret Wake with Hybrid Flow Control

Stanislav Gordeyev, Eric Jumper,

Department of Aerospace and Mechanical Engineering,

University of Notre Dame, Notre Dame, IN 46556

Bojan Vukasinovic, Ari Glezer,

Woodruff School of Mechanical Engineering,

Georgia Institute of Technology, Atlanta, GA 30332-0405

Valdis Kibens

The Boeing Company, MC S111-1240,

P.O. Box 516, Saint Louis, MO 63166

This paper presents the optical results of using hybrid, that is combined passive and active flow control to improve the aero-optical environments around a conformal-window, hemisphere-on-cylinder turret. Several wavefront sensors were used to directly measure optical distortions at several back-looking angles. It was shown that the hybrid flow control significantly reduces levels of optical distortions for elevation angles as high as 148 degrees at M = 0.3. The paper also devotes considerable attention to overcoming environmental conditions present in large-scale wind tunnels.

Nomenclature

a = POD mode amplitude

A = aperture mask (=1 inside aperture, =0 outside aperture)

C_μ = jet momentum coefficient

D = turret diameter

f = normalized differential intensity, defined in (3)

G = Green's function

I = beam intensity profile

I_0 = beam intensity inside aperture

k = $2\pi/\lambda$, laser wavenumber

M = Mach number

n = POD mode number

$\vec{n}$ = optical window outward normal vector

$\mathrm{OPD}_{\mathrm{rms}}$ = root-mean-square of OPD

R = wavefront cross-correlation function

Re_D = Reynolds number based on D

SR = Strehl Ratio

St_D = Strouhal number based on D

W = wavefront

$x, y, \vec{x}, \vec{r}$ = aperture-based coordinates

z = $x + iy$

Z = distance along the laser beam

γ = elevation angle of optical window

δ = Delta function

ϕ = POD mode

λ = wavelength

ρ = freestream air density

ρ_{SL} = see-level air density (=1.225 kg/m^3)

* = complex-conjugate

I. Background

In the last decade or so the research in using turrets to transmit laser beams from subsonic airborne platforms has greatly intensified. While a turret provides a convenient mechanical system to point-and-track the laser beam, the wake flow behind this bluff-body turret is both turbulent and complex with many vortical structures present. These structures are known to create significant density gradients and related aero-optical distortions[1] when the laser beam is transmitted through the wake of the turret even at low transonic speeds (see [2] and references therein, for instance). Left untreated, these detrimental aero-optical effects greatly reduce the laser-beam intensity in the far-field.

An earlier investigation of the optical environment around a one-foot conformal-window turret for the range of the elevation angles between 60 and 132 degrees[3] in the zenith plane showed the level of optical distortions increases for backward looking angles above 120 degrees. To measure optical aberrations at higher elevation angles and investigate strategies to mitigate these large levels of optical distortions at high back-looking angles, as well to address Reynolds number effects and scaling issues, a two-foot conformal window turret was tested for a range of back-looking angles from 129 to 149 degrees and Mach numbers between 0.3 and 0.5[4,5]. The

turret was instrumented with static ports to measure the location of the flow separation line. Velocity profiles in the wake downstream of the turret were measured using a single hot-wire and the surface flow topology was studied with oil flow visualization. Optical measurements were performed using a Malley Probe. In order to study the mitigating effects of active flow control the turret was equipped with an array of synthetic jets upstream of the window aperture. In previous studies these actuators were shown to be effective in suppressing turbulence behind a bluff-body turret at $Re_D = 8 \cdot 10^5$ [6], as well as behind a 10-inch hemispherical turret[7], where significant suppression of turbulent fluctuations and reduction in optical distortions were observed up to $M = 0.45$. The array of synthetic jets introduces small-scale, highly dissipative structures into the attached boundary layer upstream of the window aperture. This flow actuation was shown to lead to flow-separation delay on the window's surface; up to a 10-degree delay in separation was observed to an elevation angle of 139 degrees[4]. A broad-band suppression of the turbulent kinetic energy within the near wake was also observed and in particular the energy that is associated with large coherent vertical structures was suppressed in the near wake. All these changes resulted in a significant improvement in the optical environment at all measured elevation angles and Mach numbers, down by 30-40% from the baseline, no-actuation case at M=0.3[5].

This paper, along with a companion paper[8] continues the discussion of the aero-dynamic and aero-optical environment around a two-foot, hemisphere-on-cylinder, conformal-window turret when the laser beam is propagated at backward-looking angles through the turbulent wake flow. In particular, the focus of the current paper is the effectiveness of passive and hybrid (active and passive) flow control applied to the turret in order to mitigate aero-optical effects. Earlier testing[4,5] showed that the effect of the active flow control alone was found to be the modification

of the wake structure behind the turret, which, by itself, delayed flow separation and reduced optical distortions related to separation. The purpose of the tests described here and in the companion paper[8] was to observe the effect of combining active flow with passive flow control in a hybrid flow control approach.

The companion paper reports the aerodynamic environment around the turret, when passive and hybrid flow control are applied. This paper presents results of direct optical wavefront measurements at different backward-looking angles between 129 and 148 degrees and Mach numbers from 0.3 to 0.5. This paper also contains an extensive discussion of our approach to mitigating the harsh vibrational and optical environment that exist in most wind-tunnel-testing facilities. As wind tunnels being used to came aero-optical measurements get larger, these environments get harsher. As such, we felt one of the objectives of the paper was to discuss this environment and the approaches taken to deal with it. Two wavefront sensors were used to take measurements: a Shack-Hartmann Sensor and a Distorted Grating Wavefront Sensor. Modifications to the turret to accommodate 2-D wavefront optical measurements, the optical table set-up and data-reduction approaches for both sensors are presented in Section II. The optical results for the baseline, passive and hybrid flow controls are discussed in Section III. Conclusions and final remarks are presented in Section IV.

II. Experimental Set-Up

Turret geometry and design

Optical measurements for the hemisphere-on-cylinder turret were performed in the Subsonic Aeronautical Research Laboratory (SARL) indraft wind tunnel at Wright-Patterson AFB. The tunnel test section is 7 feet by 10 feet with corner fillets; the tunnel's maximum Mach number is approximately 0.5. The initial obstacle to making aero-optical measurements was that the

original tunnel side-wall windows were found to be too-poor an optical quality to perform large-aperture-beam wavefront measurements; to mitigate the problem some of the windows were replaced with optical-quality BK7 windows prior to this investigation. Although interchangeable with any of the windows shown on the left vertical wall in the top picture in Figure 1, eight of the centermost windows shown contained the new high-optical-quality windows.

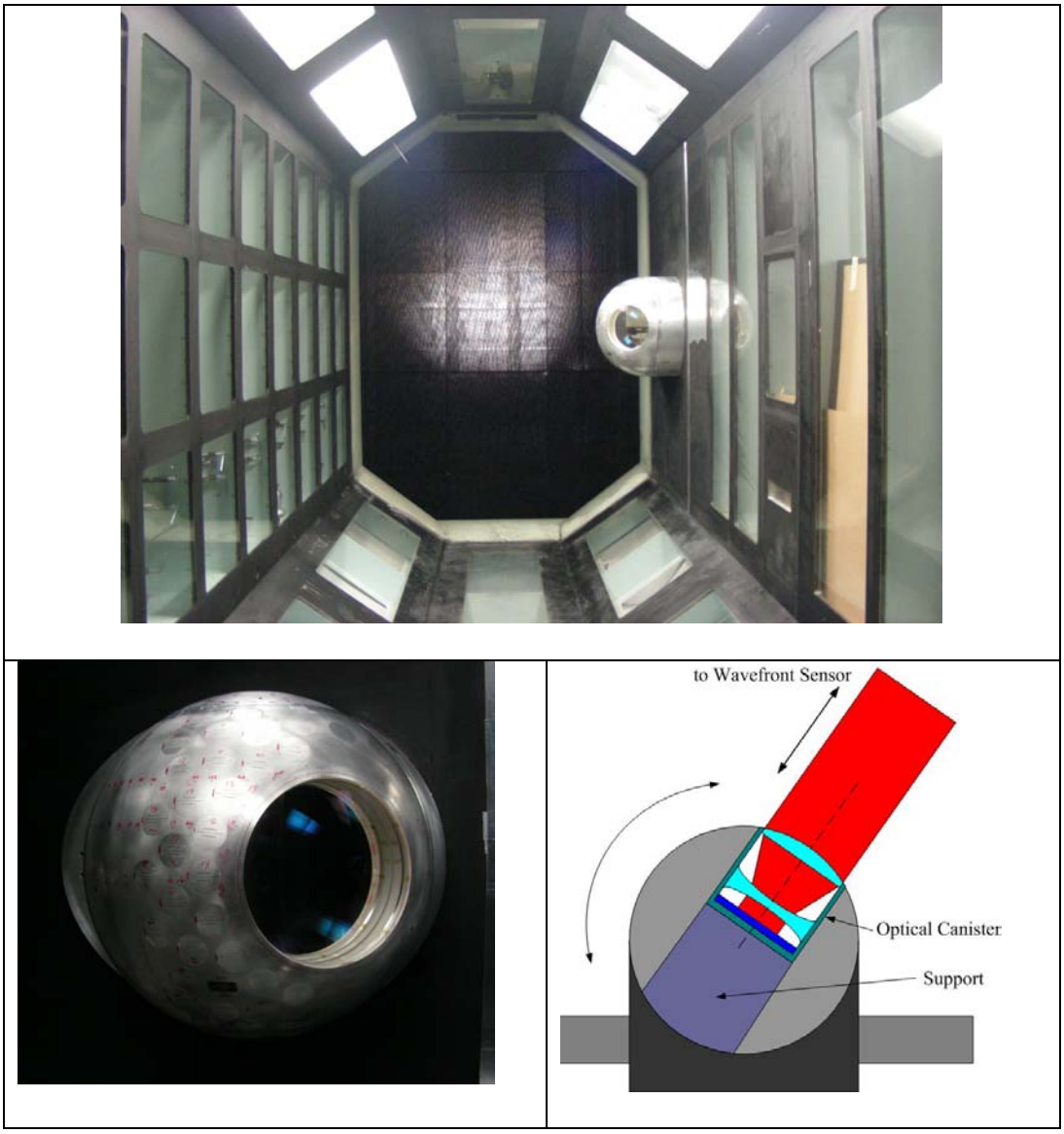

Figure 1. Top: The tunnel test section with the turret mounted on the side wall. Bottom left: The turret with the optical canister. Bottom right: a schematic of the optical canister.

The turret used in this investigation was essentially the same turret previously studied in [4,5] with the addition of an optical canister designed specifically to allow the 2-D wavefront measurements of a ten-inch laser beam. The turret had a cylindrical base 0.61 m in diameter and 0.2 m in height with a hemispherical top 0.61 m in diameter (i.e., the two-foot turret). The turret was instrumented with 122 static pressure ports, see the companion paper[8] for a detailed description of port locations, as well as a description of the single hot-wire measurements of velocity profiles in the wake downstream of the turret. The turret was installed in the side of the tunnel opposite the optical side-wall windows approximately 1 m downstream of the end of the contraction inlet, see Figure 1, top picture. The tunnel blockage imposed by the turret was 4.2%.

The optical canister with a 10-inch clear aperture was mounted into the turret, see Figure 1, bottom pictures; the canister's outer lens had a spherical outer surface, matching the curvature of the turret. Compensating optical components inside the canister were specially designed so the overall optical performance of the canister was equivalent to a flat mirror. A similar optical-canister design was successfully used to measure optical distortions around a smaller conformal-window turret[3].

Partition Plates as Passive Flow Control Devices

For these tests two passive flow control partition plates made of aluminum were attached to the turret at the transition line formed by the cylindrical base of the hemisphere. The earlier tests on the hemispherical turret[9] showed that when a partition plate is placed at the cylinder-hemisphere junction, a second necklace vortex forms at the corner of the turret-plate junction. This second necklace vortex moves the forward stagnation point on the hemispherical portion of

the turret upwards and also adds downwash motion to the wake downstream of the turret. These effects lead to separation delay of the boundary layer from the turret.

The two partition plates tested had elliptical arcs as their leading edges with their major elliptical axis in the streamwise direction and their minor elliptical axis in the crosstream direction with a circular arc for their trailing edges matching the turret cylindrical base, see Figure 2. The small partition plate extended 15 cm from the turret and the large partition plate extended 30 cm. A small gap between the plate and the turret prevented the mechanical vibration of the plate itself from transferring to the turret. The gap was taped during tests to stop air leakage through the gap.

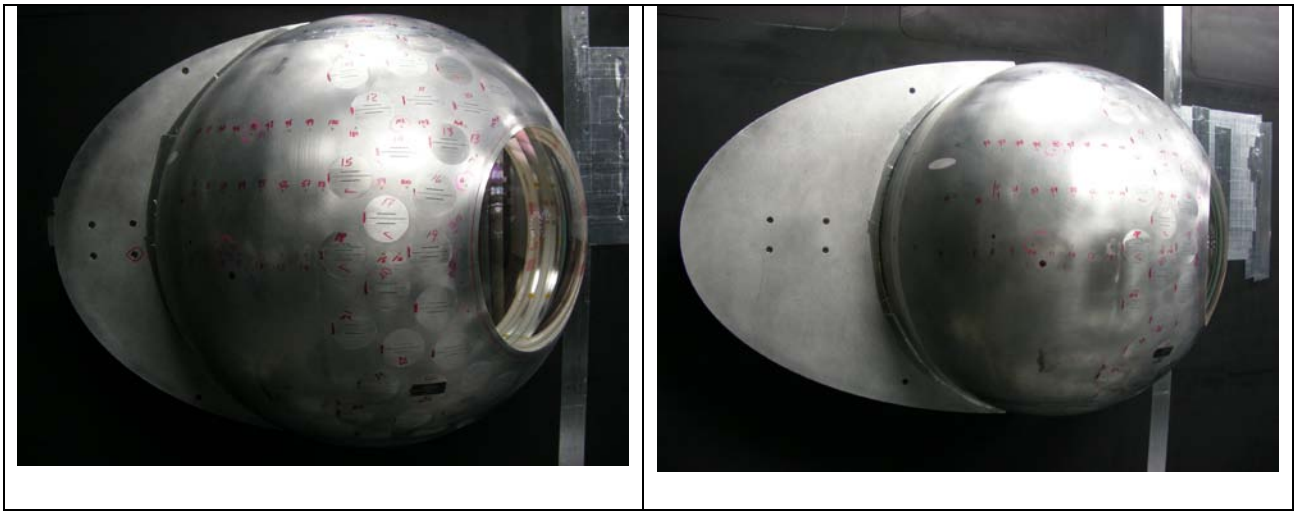

Figure 2. Small (left) and Large (right) partitions plates installed on the turret as tested passive flow control devices.

Active Flow Control

As mentioned in the introduction, active-flow actuators were mounted on the surface of the turret. The actuators' principle of operation is described in [4,8]; they were zero-mass, blowing-suction type piezo actuators, often referred to as synthetic jets[10]. In preliminary studies[4,5] these

actuators (although at a slightly different arrangements) were shown to delay the separation point and dissipate small-scale structures behind the turret with a corresponding reduction in the level of optical distortions by as much as 40% at M = 0.3. The actuators were flush-mounted with the turret surface around the conformal window's edge, see Figure 3; a total of 36 individually-addressable actuators were distributed primarily upstream of the window aperture, see [8] for the complete description of the actuators' locations. The actuators' slit orifices were oriented along the local free stream, injecting streamwise vorticity into the boundary layer. As described in [4,8], these actuator devices create high-frequency (St_D ~ O(10)) vortex pairs to introduce small-scale structures into the boundary layer upstream of the aperture. These structures interact with the boundary layer and postpone the shear layer formation to further downstream from its unactuated (baseline) location and promote higher dissipation rates in the separated wake. As a result, the pressure and density fluctuations in the wake are reduced, resulting in an improvement of the optical environment at back-looking elevation angles.

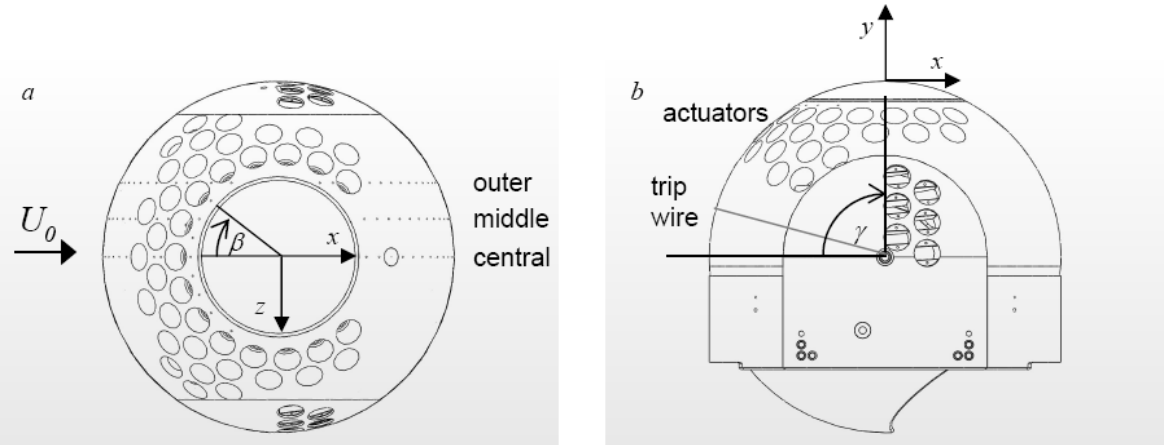

Figure 3. Top (*a*) and side (*b*) views of the turret model with actuators (from [8]).

The actuators were operated with a suction-blowing frequency of 1.6 kHz, the natural frequency of the piezo-electric diaphragms used in the actuators. This actuation frequency

corresponds to St_D = 9.8 at M = 0.3. Several combinations of actuations were tested. In this paper the results for only one case is reported, labeled case AC1 in [8]. This case, referred to hereafter as "Case 1", made use of all 36 actuators at their highest jet momentum coefficient C_μ = $6.5 \bullet 10^{-4}$. Further, only the results for M = 0.3 for the Case 1 arrangement is reported.

Optical table set-up

The optical environment around the turret at different elevation angles and the impact of the passive and active flow control were investigated using two wavefront sensors (WFS). One sensor was a Distorted Grating WFS (later referred as DGWFS), and the other sensor was a 2-D Shack-Hartmann WFS (later referred as 2-D WFS). Optical measurements were taken only in the zenith plane, i.e., azimuthal angle of 0 degrees for elevation angles γ = 129°, 137°, 143°, and 148° (the elevation angle is defined in Figure 4) at three Mach numbers M = 0.3, 0.4, and 0.5.

To support the optical table, a series of trusses were built and were attached to a side wall of the tunnel. To reduce mechanical vibrations from the tunnel walls, the optical table was rested on a platform using 12 vibration-isolation boots. The schematic of the optical lay-out is shown in Figure 4. A one-inch continuous (CW) He-Ne laser beam was expanded to a 10-inch collimated beam using a 10-to-1 custom-made off-axis reflective telescope; using two 12-inch steering mirrors, the 10-inch beam was forwarded through the optical windows on the instrumentation side of the tunnel into the test section with the turret installed on the opposite wall. The 10-inch beam traveled through the flow around the turret, entered the optical canister and was reflected back co-axially, traveling through the same flow again (thus increasing the signal-to-noise by a factor of two) and came back to the optical table. After being contracted to the one-inch beam by the 10-to-1 telescope, the return beam was reflected out of the original beam train using a cube beam-splitter. After passing through an optical-relay system, the beam was directed onto a Fast

Steering Mirror (FSM). The purpose of the FSM was to remove low-frequency jitter from the incoming beam due to tunnel vibrations; this vibration was present even with the isolation boots in place. The FSM used a closed-loop control system described in detail in the following section. After the FSM, the beam was split into two beams using a plate beam splitter. One beam was focused on a Tip/Tilt Quad Cell, which was a part of the FSM closed-loop control system; the second beam was directed onto the DGWFS sensor.

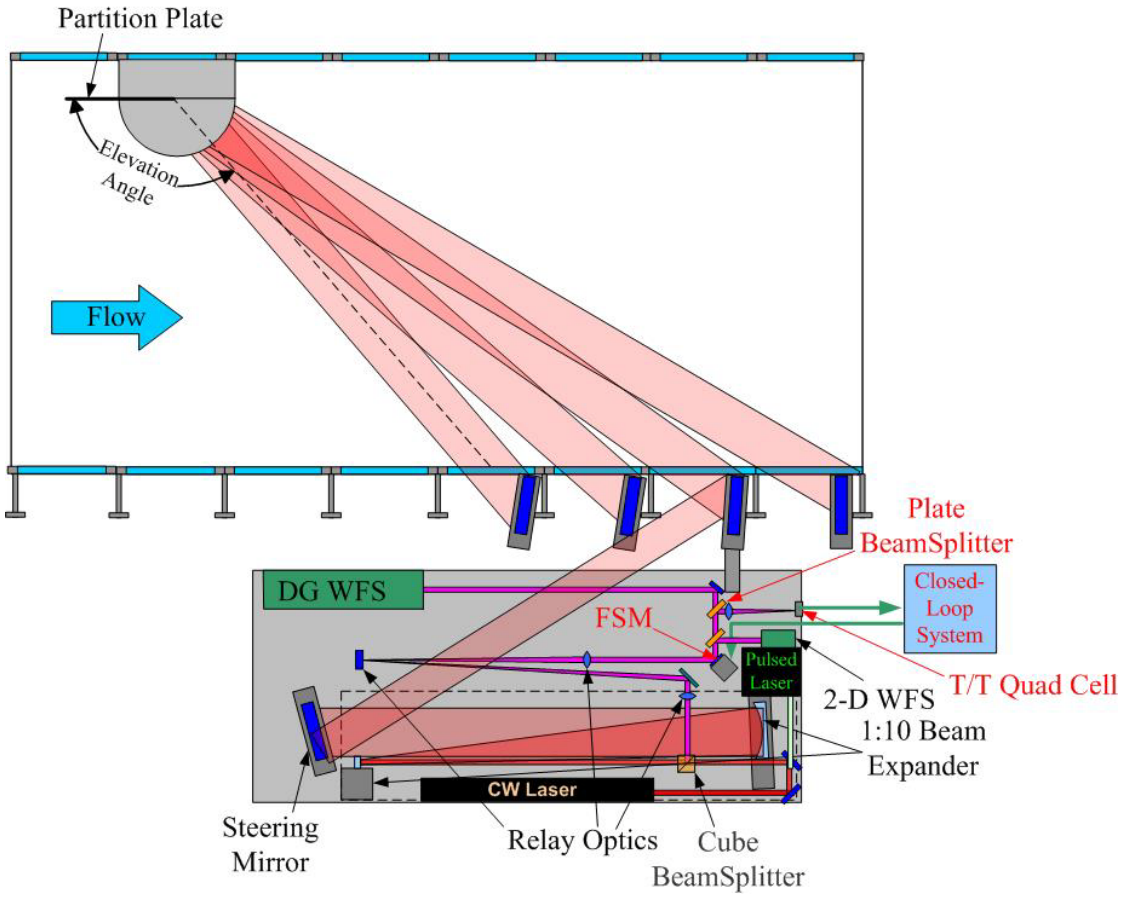

Figure 4. Optical lay-out with DGWFS and 2-D WF sensors. FSM System components are marked in red letters.

To take wavefront measurements using the 2-D WF sensor, a second, pulsed frequency-doubled Nd:YaG laser was used. Due to the sensor low sampling rate (~10 Hz), the sensor collected a series of uncorrelated snapshots of wavefronts.

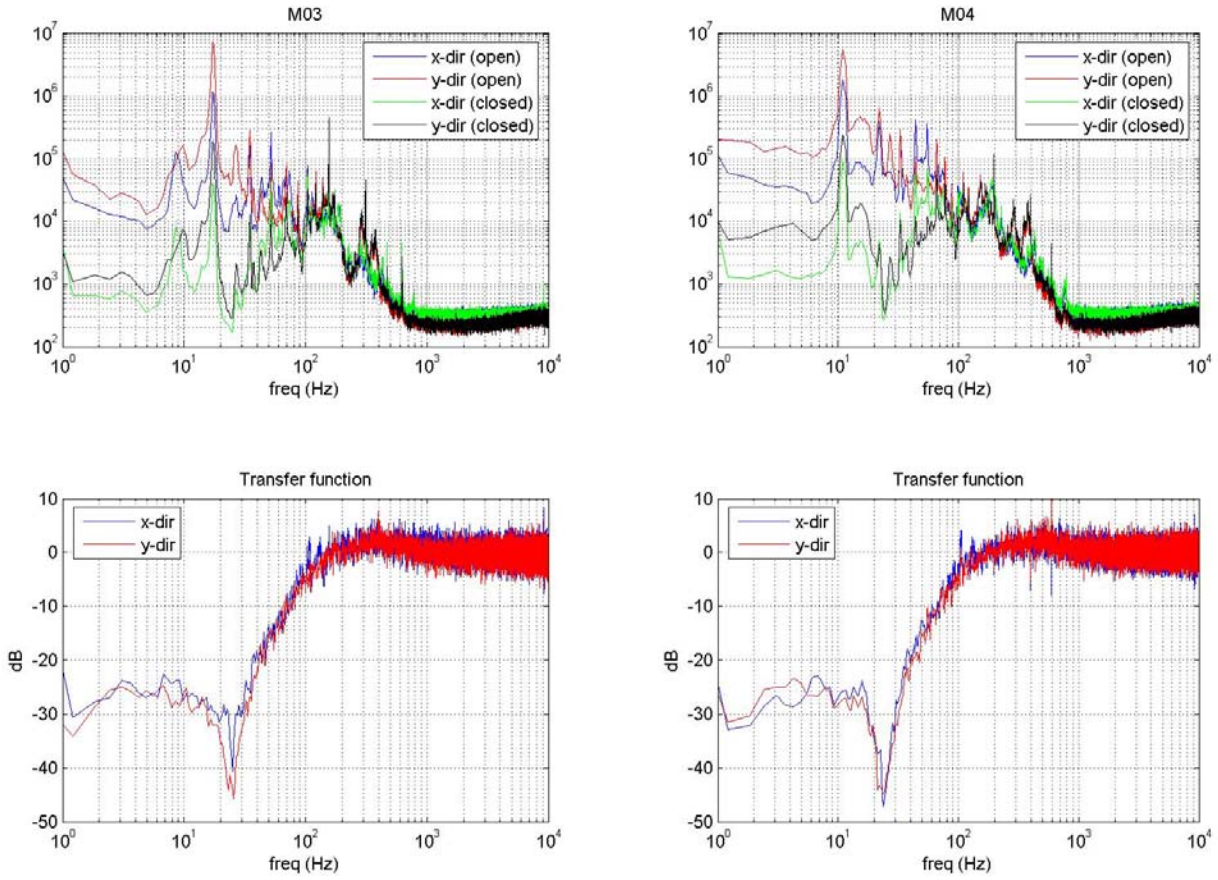

Figure 5. Top plots: Beam jitter spectra for open and closed-loop system for different Mach numbers. Bottom plots: FSM closed-loop transfer function.

For each elevation angle the optical table was moved to a different location along the sidewall of the tunnel and the steering mirrors were re-aligned. During the measurements, the red laser and FSM system were turned on and wavefronts were measured by the DGWFS. Then the red laser was turned off, the green laser was switched on and wavefronts were collected by the 2-D WFS. The FSM system was turned off when the 2-D WFS was used.

The optical windows on the side wall were 18" wide, so the largest theoretical elevation angle at which a 10"- beam can pass through the window unclipped is γ_{max} = 180 - *asin*(10"/18") = 146 degrees, but the support I-beams around the test section and the large steering mirrors forced the

beam to be clipped at smaller elevation angles, see Figure 4. For these experiments, the only elevation angle with no beam clipping was 129 degrees; the beam was clipped for all other elevation angles. The clipping was as large as half of the aperture at the largest elevation angle of 148 degrees.

Effectiveness of Closed-Loop FSM system

Tunnel-induced mechanical vibrations in the SARL facility presented a difficult problem in taking and reducing optical data. During previous turret tests in SARL using a Malley probe a vibration-isolation system consisting of inner-tubes was used[5]. For the current tests the optical table was isolated from most of the tunnel-induced high-frequency vibrations (~50-300 Hz) using vibration-isolation boots; however, it was discovered that some low frequencies, notably in the range of 10-20 Hz were still present on the optical table and all optical components. To remove these residual vibrations a Fast Steering Mirror (FSM) and concomitant closed-loop, beam-stabilizing system was used.

To test the effectiveness of the FSM system, the overall jitter signal was measured by the Tip/Tilt Quad Cell with the FSM loop open and closed. Results for M = 0.3 and 0.4 are given in Figure 5. The top plots show jitter spectra in x-(parallel to the table) and y- (normal to the table) directions for the open- and the closed-loop for M = 0.3 (left column) and M = 0.4 (right column). The bottom plots in Figure 5 show the transfer function, which is the ratio between the jitter amplitude between the closed- and the open-loop as a function of frequency. As shown in the Figure 5, the FSM system greatly suppressed the jitter amplitudes (by more than 10 dB) for all frequencies below 100 Hz. The standard deviations of the beam jitter for the open- and the closed-loop are shown in Figure 6. For all Mach numbers the FSM closed-loop system kept the overall beam jitter to be less than 30 microradians. Nevertheless, even with the FSM system

there were dominant peaks in the beam jitter at 10 and 20 Hz, although greatly reduced from the no-FSM case.

This closed-loop system relies on an analog T/T Quad Cell to measure and remove the vibration-related tip/tilt from the returning laser beam; thus, the system required a *continuous wave* (CW) laser to operate. The DGWFS also relied on a CW laser to take wavefronts; thus, the two systems could act simultaneously.

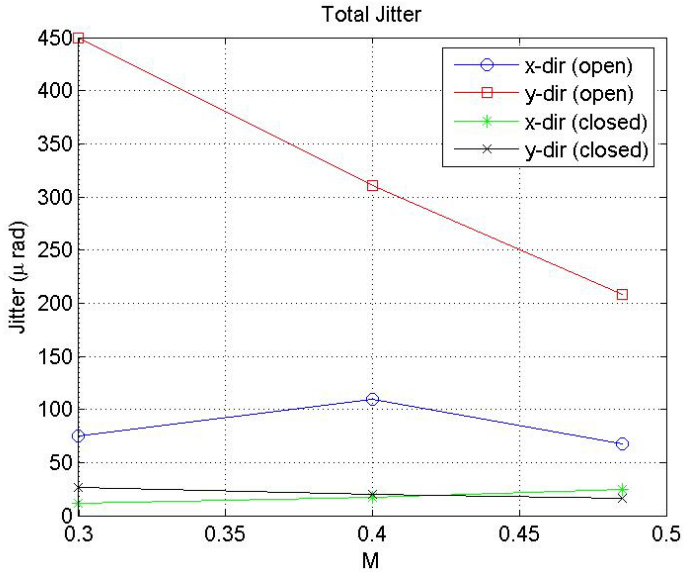

Figure 6. Overall standard deviation of jitter with FSM system. Open loop - system is off, Closed loop-

DGWFS principle of operation and data reduction

The principle of operation of Distorted Grating WFS (DGWFS) is described in detail in [11-13] and only essential information will be given here. The DGWFS relies on the Intensity Transport Equation, Eq.(1), which describes how intensities at different distances, *Z*, along the beam, $I(\vec{r})$, are related to the wavefront, $W(\vec{r})$, for a given wavenumber, *k*.

$$-k\frac{\partial I(\vec{r})}{\partial Z} = \nabla\cdot[I(\vec{r})\nabla W(\vec{r})] = I(\vec{r})\nabla^2 W(\vec{r}) + \nabla I(\vec{r})\cdot\nabla W(\vec{r}) \qquad (1)$$

Consider for simplicity a uniform-intensity beam, $I = I_0 A$, where *A* is unity inside the beam and zero outside the beam; the intensity gradient becomes $\nabla I = -I_0\delta_C\vec{n}$, where δ_C is the Delta-function along the beam boundary and $\vec{n}$ is the outward normal vector. Thus, Eq. (1) can be simplified to,

$$-k\frac{\partial I(\vec{r})}{\partial Z} = I_0 A\nabla^2 W(\vec{r}) - I_0\delta_C \vec{n}\cdot\nabla W(\vec{r}) \tag{2}$$

This equation shows that the change in the intensity along the beam is proportional to the local wavefront curvature (the first term in right-hand-side of Eq. (2)) and the change in the beam shape depends on the local wavefront slope on the beam boundary (the second term in right-hand-side of Eq. (2)).

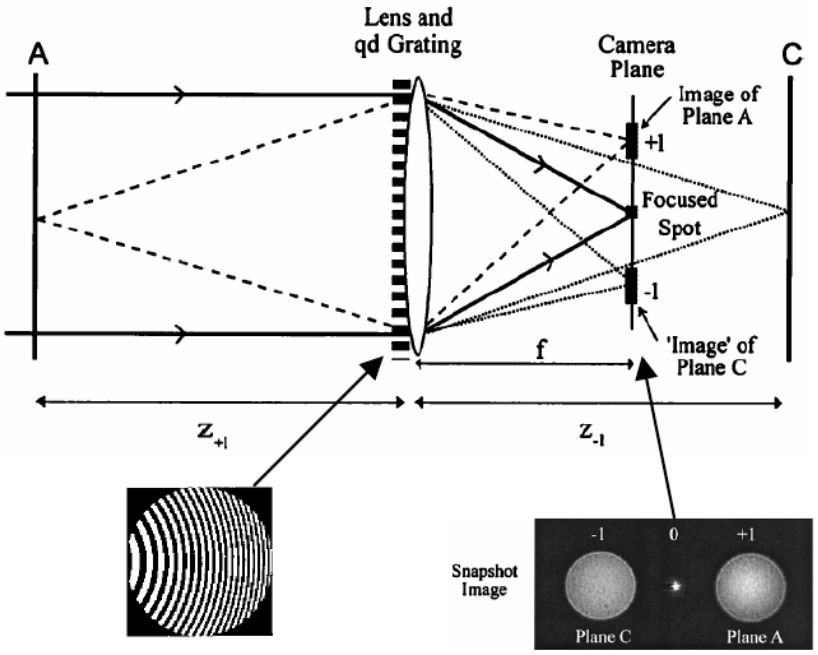

Figure 7. Schematic of the optical system used for distorted grading wavefront sensing (top) and an example recorded image (bottom right) (From [11]).

One way to simultaneously record intensities at two different *z*-planes is to use a quadratic grading combined with a lens [11], see Figure 7. It creates a pair of images corresponding to beam intensities at known distances z_1 and z_2 which are defined by the lens-grating geometry. In addition, the image has a central focused spot, which is irrelevant to the measurements.

Subtracting one image from another and knowing the distance between image planes, $\Delta Z=Z_1-Z_2$, the left-hand-side term in Eqs. (1) or (2) can be approximated as $\frac{\partial I(\vec{r})}{\partial Z} \approx \frac{I_{Z1}(\vec{r}) - I_{Z2}(\vec{r})}{\Delta Z}$. Equation (2) can be solved iteratively [14,15], by expanding the solution into Zernike polynomials [13] or by applying a Green's function approach [12]. The Green's function approach was used to reduce data from DGWFS in this test.

The DGWFS data for each set were reduced as follows,

1. Images were recorded at a sampling rate of 20 kHz for 4 seconds.
2. After aligning the images were subtracted from each other to get the approximate a normalized differential intensity,

$$f(\vec{r}) = \frac{1}{I(\vec{r})} \frac{\partial I(\vec{r})}{\partial Z}. \tag{3}$$

3. A complex Green's function for a round beam was applied to compute wavefronts,

$$W(z = x + iy) = \int_{|z|<1} G(z,\xi) f(\xi) d\xi \text{ with } G(z,\xi) = \frac{1}{2\pi} \ln|z-\xi| + \frac{1}{2\pi} \ln|1 - z\xi^*|. \tag{4}$$

4. A steady wavefront was calculated by averaging all wavefronts in time and this was subtracted from each wavefront.
5. Tip/Tilt was removed from each wavefront.
6. Data were high-pass filtered with a cut-off frequency of 50 Hz to remove effects from spurious 10-Hz and 20-Hz peaks present in the incoming laser beam.

As discussed later, this data treatment was only partially successful in returning acceptable wavefront data. Additional post-process analysis will be presented in the Section III.

2-D WFS data reduction

As mentioned in the previous section, DGWFS relies on the continuous laser to take advantage of the FSM system. On the other hand, the 2-D WFS needs a *pulsed* laser to take a series of uncorrelated wavefronts and unfortunately in the set-up used for this test series the 2-D WFS could not take advantage of the FSM system to remove relatively-large, low-frequency tip/tilt present on the incoming laser beam. Without the FSM, if left untreated, these large tip/tilts would spatially alias and corrupt the 2-D WFS data; therefore an optical set-up involving the 2-D WFS was designed to remove most of wavefronts with large tip/tilt angles from the data. To do this, a small iris was placed at the focal plane of the last contraction telescope, where the tip/tilt results in a lateral beam displacement, see Figure 8. This small pinhole-like iris blocked the laser beam with large tip/tilt, allowing only beams with small tip/tilt to go through the iris and reach the sensor. Therefore, large tip/tilt resulted in a no-light frame taken by the 2-D WFS, which was subsequently discarded during the post-process analysis. This simple approach allowed us to take tilt-uncorrupted wavefronts using the pulsed laser set-up even when the vibration-induced beam jitter was not removed by the FSM; however, this approach also resulted in a dramatic decrease in the ratio of usable wavefronts to the total number of wavefronts taken. At M = 0.3, for example, the usable-frame ratio was found to be 20-30% of the total taken; this dropped to less than 5% of good frames at M = 0.5, when levels of beam jitter were the greatest.

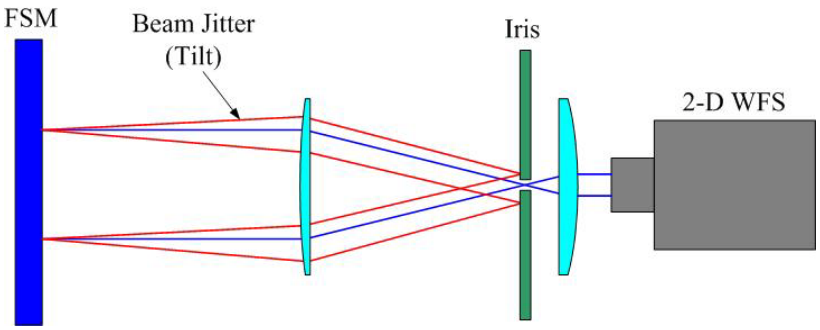

Figure 8. Schematic of removing large tilts from 2-D WFS optical set-up.

Besides the large tip/tilt corruption, described above, there was also another source of wavefront corruption. The main laser was expanded to a 10-inch diameter beam and traversed more than 5 m before entering the tunnel, see Figure 4. After bouncing off the turret and returning through the tunnel windows, the laser beam again traveled 5 m before it was reduced to a one-inch beam on the optical table. While traveling through these distances the laser beam was distorted by small temperature fluctuations present in the ambient air around the tunnel. These "ambient-air" optical aberrations were *not related* to the optical aberrations of interest (that is, the optical distortions caused by the turbulent flow around the turret), yet they were imbedded on most wavefronts measured. One way to separate these distortions from the distortions-of-interest is to recognize that the former distortions move across the aperture with very slow speeds (less than a meter per second), while the latter ones travel at approximately the speed of the tunnel flow (more than 100 m/sec). As such, a high-pass filter applied to wavefronts, *sampled at high frequency* with those taken with DGWFS can effectively separate these "not-of-interest" aberrations. But the 2-D WFS takes frames at 10 Hz, which is not high enough to use the high-pass filter approach. Thus, another method was used to select wavefronts with the least amount of unwanted "ambient-air" aberrations, thus minimizing the level of wavefront corruption.

The method of choosing wavefronts with a minimal "ambient-air" corruption relies on the fact that the characteristics or scales of "ambient-air" aberrations are quite different from those present in "aero-optical" aberrations. The wavefront measurement of "no-flow" cases, when the tunnel was off and the aberrations were only due to "ambient-air," showed that the "ambient-air" wavefronts typically have relatively large-scale variations, while "aero-optical" aberrations are usually caused by small, compact structures present in the separated shear layer behind the turret[3]. Once in a while the ambient air is relatively still along the beam path, resulting in

minimal aberrations from the "ambient-air"; therefore, when the "ambient-air" corruption is present, the wavefront has mostly "low-order" components, like defocus, astigmatism, coma etc., see an example in Figure 9, left image. If the ambient-air happens to be relatively quiet at a particular moment, only small-scale variations in the wavefront from aero-optical effects will be present, see Figure 9, right image.

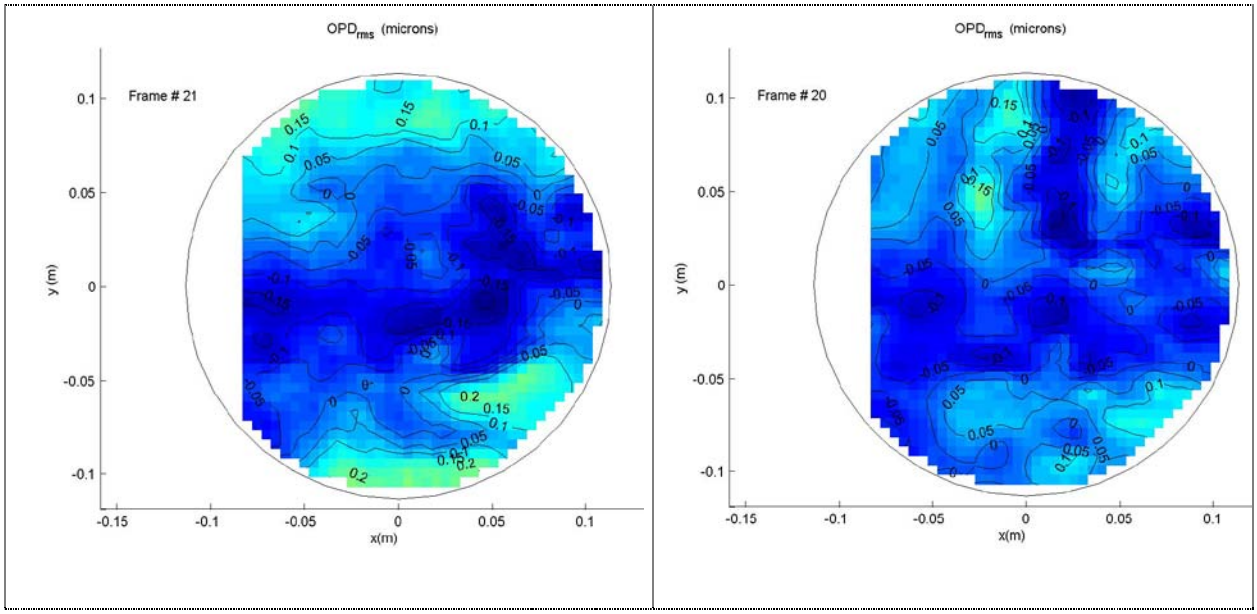

Figure 9. Left image: a wavefront with large de-focus and astigmatism present, indicating corruption from "ambient-air". Right image: a wavefront with only small, shear-layer structures present. Elevation angle is 137 degrees, M =0.3.

Based on these observations, wavefronts with no significant large-scale aberrations were selected for subsequent post-analysis. It is important to mention that the described wavefront selection is somewhat subjective and relies on *a priory* knowledge of the spatial distribution of the aberrations; however, while some physically-related wavefronts might be left out during this selection procedure, it significantly reduced the "ambient-air" corruption effects.

For each test run, the 2-D wavefronts were processed as follows:

1. 300 wavefronts were taken for each run.
2. “No intensity” (frames blocked by the iris) frames were removed from the data set.
3. Tip/tilt and piston components were removed from each remaining wavefront.
4. Wavefronts with only small-scale structures were selected from each sub-set.
5. The ensemble-averaged spatial OPDrms was calculated for all remaining wavefronts for each run.
6. Error bounds were also calculated for each data point.

III. Optical Results

2-D WFS results

As discussed above, the iris was used to remove wavefront frames with large tip/tilt values, which resulted in a dramatic decrease in ratio of good WFs to the total number of WFs taken. For M = 0.3 the good-frame ratio was found to be typically 20-30%, dropping to less than 5-10% of good frames at M = 0.5, when mechanical vibrations were the largest. The additional down-selection of wavefronts with a minimal “ambient-air” corruption further reduced the number of suitable wavefronts to analyze. For Mach number of 0.3 the number of good frames per test case was between 15 and 60; at M = 0.4 and 0.5 ever fewer good frames were left, making statistics unreliable for the M = 0.4 and 0.5 data. Therefore, results for only M = 0.3 will be presented in this paper.

In [2] it was shown that, if the Reynolds number is higher than 200,000-500,000, for geometrically-similar turrets and elevation angle, the optical data should scale as

$OPD_{rms} \sim (\rho / \rho_{SL}) M^2 D$, where ρ_{SL} is the reference sea-level density. Therefore, all optical data in this paper are presented in the normalized form, $\frac{OPD_{rms}}{(\rho / \rho_{SL}) M^2 D}$.

Figure 10 presents normalized values of temporally-averaged, spatial root-mean-square of wavefronts, for the baseline cases (no AFC) for M = 0.3 calculated from wavefronts collected by 2-D WFS. Results using the Malley Probe taken on the same turret in the previous studies[5] are also presented for comparison. For the baseline case without partition plates, values of OPDrms measured using the Malley probe compare quite well with results from the 2-D WFS. Levels of optical distortions increase with the elevation angle, from approximately $1.5(\rho/\rho_{SL})M^2D$ at 129 degrees to $2.3(\rho/\rho_{SL})M^2D$ at 148 degrees. Note relatively big error bounds for 2-D WFS results due to the small number of "good" frames used from 2-D WFS data. At the 143 degree case the iris was not used, so the 2-D WFS wavefront data were corrupted by large tip/tilt, and, even after significant efforts to "clean-up" the data it was concluded that the data at this angle were unreliable and they are not shown here. Also, data for the large partition plate at the elevation angle of 130 degrees were found to be significantly corrupted and not included here.

An addition of the small partition plate to the turret resulted in a decrease in the levels of optical distortion at elevation angles of 137 degrees by 11% and 148 degrees, by 16%. As discussed in detail in the companion paper [8], the partition plate moves the stagnation point upwards in front of the turret, which resulted in delaying the flow separation from the turret by more than 10 degrees compared to the baseline flow. As a consequence, the delayed separation moved the optically-active region behind the turret to a higher elevation angle. This effect is even more pronounced when the large forward partition plate was installed, reducing levels of optical distortions by 22% and by 33% at the elevation angle of 148 degrees. With the small partition plate, OPDrms were observed to be slightly increased at the elevation angle of 129

degrees for reasons not quite understood; it should be noted that there is a possibility that anomalous behavior at 129 degrees might be an artifact of not having enough wavefronts to compute converged statistics at this angle. Also, it is interesting to note that global flow topology around the turret with either the small or the large partition plate was found to be almost identical[8], yet there is a clear distinction between plate effects in terms of improving optical distortions behind the turret.

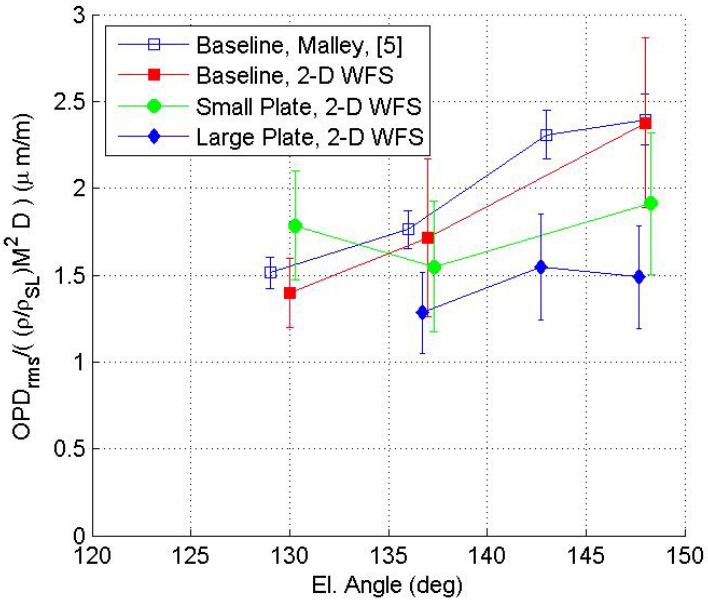

Figure 10. Normalized 2-D WFS optical results for different partition plate configurations without AFC.

When only AFC was activated, it also reduced levels of the optical distortions. Figure 11 showed OPDrms from 2-D WFS for the baseline and AFC, Case 1. OPDrms was reduced by 22% at 137 degree and by 8% at 148 degrees. These results are consistent with the optical results measured with the Malley Probe, when similar levels of AFC-related reduction were observed.[4]

When hybrid control, that is AFC combined with partition plates, was applied, it significantly reduced the levels of optical aberrations at the elevation angles 137, 143 and 148 degrees, see Figure 11. At 137 degrees, the combination of the small forward partition plate and AFC, Case 1, reduced OPDrms by 22%. The large-partition-plate hybrid control showed similar reductions at this elevation angle. At 143 degrees, the large-partition-plate hybrid control reduced OPDrms to$1.3(\rho/\rho_{SL})M^2D$. Finally, at 148 degrees, both the small and the large partition plates combined with AFC, Case 1, lowered the levels of optical aberrations by 42%.

It is interesting to observe that when hybrid control is applied, regardless of the size of the partition plate the levels of optical distortions become approximately independent of the elevation angle, with OPDrms between $1.3(\rho/\rho_{SL})M^2D$ and $1.4(\rho/\rho_{SL})M^2D$ for the range of the elevation angles between 137 and 148 degrees. Static pressure distributions for the hybrid control showed that the flow was found to be fully attached upstream of the aperture for all measured elevation angles.[8] It is known that it takes some angular distance downstream of the separation point, typically on the order of 10-15 degrees, for shear-layer structures to develop and become optically active [3]. The hybrid control moves the formation of these structures to a higher elevation angle and shear-layer structures will form either downstream of the aperture for smaller elevation angles or only by the end of the aperture at the highest elevation angle of 149 degrees. As shear-layer structures are the main source of the optical aberration, the resulting optical distortions with hybrid control were significantly less compared to the baseline distortions, as would be expected from their effect on separation.

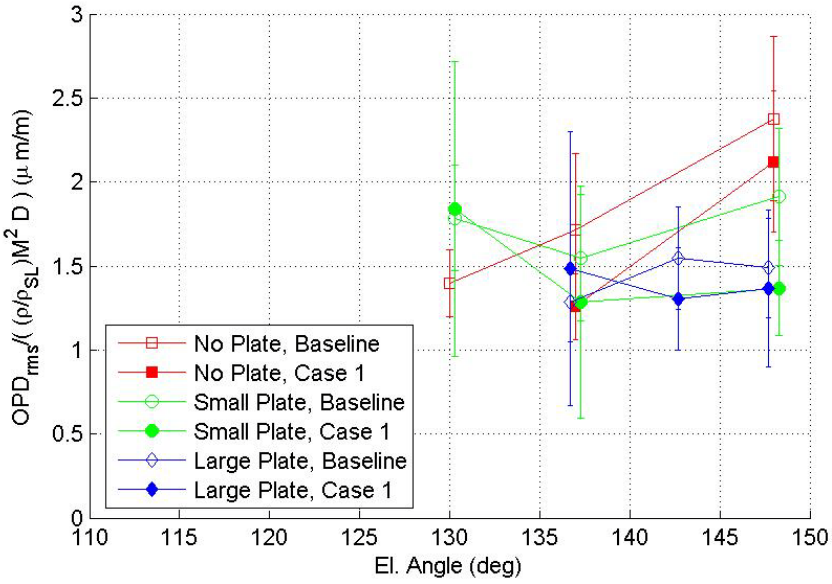

Figure 11. Normalized 2-D WFS optical results for Baseline and AFC, Case 1 for different partition plate configurations.

Another, although weaker contributor to the optical distortions is the attached boundary layer upstream of the separation over the portion of the aperture, which is assumed to be largely unaffected by the flow control. Boundary-layer optical mitigation control could possibly further improve the optical environment around the turret at these elevation angles.

Finally, for 2-D WFS results for 130 degree elevation angle (Figures 10 and 11) at M = 0.3 neither addition of partition plates nor different actuations improved the optical environment. The small partition plate made it slightly worse. Overall, the flow control was found to be ineffective at this angle. One possible reason is that the actuators were located too far upstream from the separation line and therefore had a lesser effect on modifying the separation region. Another reason might be that the flow in the baseline case was attached at this point so that the optical distortions are due to the attached boundary layer over the aperture and actuators are ineffective in reducing these aberrations.

DGWFS results

The DGWFS data were reduced as described above and the results for passive flow control are compared with 2-D WFS results in Figure 12. Generally, the results agree well, except for the large partition plate at the elevation angles of 137 and 143 degrees, where the optical distortions measured by DGWFS were more than twice as high as the OPDrms measured by 2-D WFS. Visual inspection of wavefront "movies" (i.e., time-ordered successive wavefront frames) at these points revealed that these wavefronts exhibited sudden "jumps" where the wavefront changed abruptly between adjacent frames. The sampling frequency was 20 kHz, so these "jumps" cannot be explained by under-sampling, since the time interval between frames (1/20 kHz = 0.05 msec) is much smaller than a typical convection time over the aperture of approximately 2 msec (the aperture size, 0.2 m, divided by the freestream speed of 100 m/sec).

In order to investigate the nature of these "jumps", the DGWFS data were decomposed into a series of spatial orthogonal modes using the POD analysis[16,17] as

$$W(\vec{x},t) \approx \sum_{n=1}^{N} a_n(t)\phi_n(\vec{x}), \tag{3}$$

where spatial modes, $\phi_n(x,y)$, are computed solving the integral equation,

$$\int R(\vec{x};\vec{x}')\phi_n(\vec{x}')d\vec{x}' = \lambda_n\phi_n(\vec{x}) \tag{4}$$

with the 2-point spatial correlation matrix, $R(\vec{x};\vec{x}') = \overline{W(\vec{x},t)W(\vec{x}',t)}$ as the kernel. The temporal coefficients were found by projecting the wavefronts onto each corresponding spatial mode,

$$a_n(t) = \int W(\vec{x},t)\phi_n(\vec{x})d\vec{x}\,. \tag{5}$$

The first N = 100 modes were kept in the expansion, Eq. (3), with more than 99.9% of "optical energy" captured.

Temporal coefficients for the first three POD modes for the large partition plate, no AFC for the elevation angle of 143 degrees are presented in Figure 13. The sudden jumps in the temporal coefficients for the first and third modes are clearly observed, while for the cases with a good agreement between sensors, these jumps were not present in the temporal evolution of POD modes (not shown). Also, average amplitudes of low-order modes were higher for data sets when "jumps" were present.

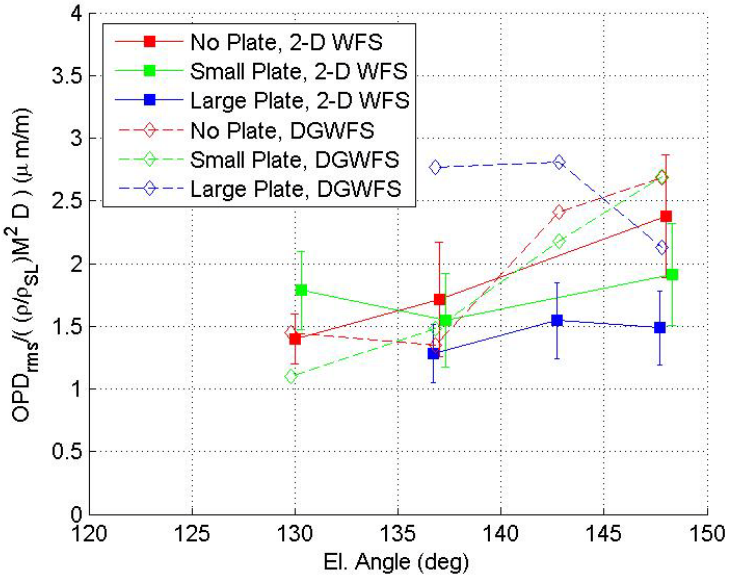

Figure 12. Normalized optical for Passive flow Control, noAFC for DGWFS and 2-D WFS.

To further investigate the origin of the jumps, the right-hand-side of Eq. (1) was calculated from the wavefront time series. The curvature of wavefront inside of the beam (the first term in r.h.s. of Eq. (1)) was found to be smoothly changing from frame to frame, while the boundary term (the second term in r.h.s. of Eq. (1)) related to the beam shape was experiencing sudden "jumps" from frame to frame. Recall that the DGWFS wavefront reconstruction involves a convolution with the *global* Green's function, see Step 3 in the DGWFS data reduction algorithm on page 16. Thus, unlike the conventional Shack-Hartmann WF sensor, which requires only

local information about the wavefront gradients, the DGWFS requires *global* information of the wavefront curvature *and* the beam shape to reconstruct wavefronts. Thus, any local errors in measuring the curvature or the beam shape [r.h.s of Eq. (1)] will corrupt the wavefront at all points across the aperture.

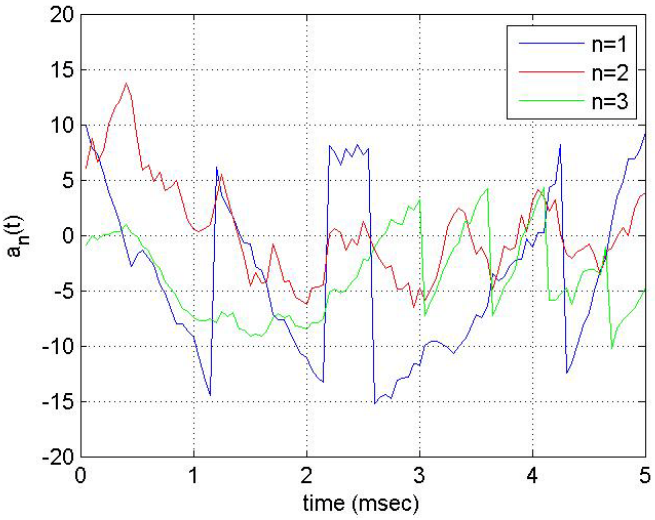

Figure 13. Temporal coefficients, $a_n(x,y)$, defined by (5) for first 3 POD modes for the large partition plate, no AFC case, elevation angle of 143 degrees.

Edges of the laser beam are typically corrupted by non-ideal optics, near-field effects (Fresnel rings near beam edges, for instance) or, more importantly by non-roundness of the beam. As was mentioned in Section II, for all elevation angles, except 130 degrees, the beam was clipped, see Figure 9, for example. When the round-beam Green's function is applied to the clipped beam, it leads to spurious low-order modes strongly coupled with the time-dependent tip/tilt component; these spurious modes are a pure artifact of an improper Green's function. All these effects, combined with a discrete-pixel nature of the CCD camera used to capture the wavefronts, are the most likely cause of the observed temporal jumps in the low-order modes.

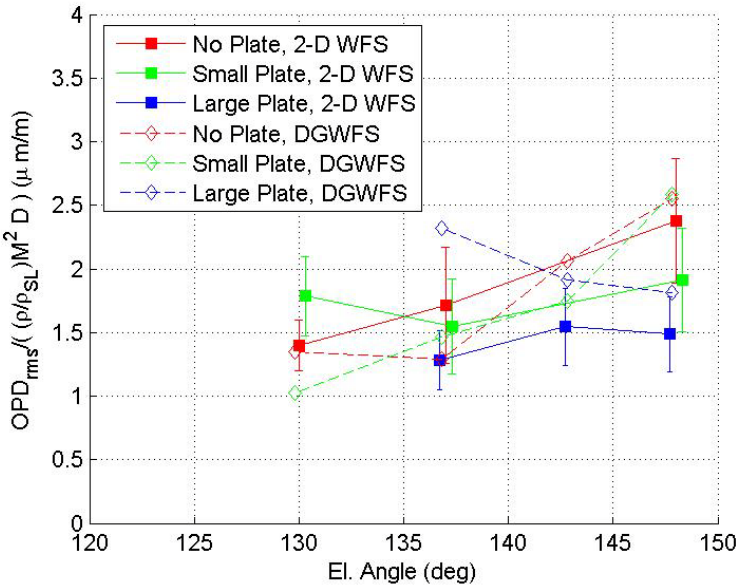

Figure 14. Normalized optical results with the removed first POD mode for Passive flow Control, no AFC for DGWFS and 2-D WFS.

Recognizing that the low-order POD modes might be significantly corrupted, the first POD mode was removed from the wavefront data, that is starting the summation from n = 2 in Eq. (3), and the resulting OPDrms are presented in Figure 14. With the first POD mode removed, DGWFS data agree better with the 2-D WFS data, presented in Figure 12, except for the elevation angle of 137 degrees. Inspection of the temporal coefficients of the POD modes at 137 degrees revealed the presence of a 200-Hz harmonic in the first several POD modes. The nature of this harmonic is not clear at this point; however, it is not physical and thus was presumed to be a corrupting effect. Once the corrupted data was removed the optical data between the two sensors compared well. Therefore, all conclusions about the WF data presented in Figure 10 remain valid fro the DGWFS data. Unfortunately, only results for the passive flow control were available from DGWFS; however, since after extensive analysis, both the 2-D WFS and DGWFS

data agree, the availability of the DGWFS data for the case where it was available add credibility to the 2-D WFS data where only the 2-D WFS data were available.

IV. Conclusions

Optical aberrations around a conformal hemisphere-on-cylinder turret 0.61 m in diameter at backward-looking elevation angles between 130 and 148 degrees for M = 0.3, 0.4 and 0.5 were directly measured using two WF sensors, a 2-D Shack-Hartmann sensor and a Distorted Grating WFS. Several active, passive and hybrid flow control strategies were tested. It was found that the hybrid control, consisting of the partition plate placed upstream of the turret combined with active flow control using distributed synthetic jets upstream of the optical aperture were successful in delaying the flow separation on the turret and consequently significantly reducing levels of optical aberrations at high elevation angles by as much as 40% at the elevation angle of 148 degrees at M = 0.3. Also, it was found that unlike the baseline (no control) case, where optical aberrations were found to be a function of the elevation angle, in the case of the hybrid control the residual aberrations were observed to be approximately independent of the elevation angle up to the highest measured elevation angle of 148 degrees. This effect was attributed to the fully-attached flow upstream of the optical window due to the hybrid control.

Reduction in the near-field OPDrms is very important, because it is directly linked to an increase in the laser intensity in the far-field. The far-field Strehl Ratio, *SR*, defined as the ratio between the far-field intensity with optical aberrations present, normalized by the maximum diffraction-limited intensity in the absence of optical distortions, can be estimated using the Large-Aperture Approximation as $SR = \exp\left(-(2\pi \mathrm{OPDrms}/\lambda)^2\right)$. Values of Strehl Ratio for the baseline and the hybrid flow control with the large partition plate for the laser wavelength of λ = 1 micron are plotted in Figure 15. These SR data were for the M = 0.3 case and a 0.61 m turret.

If the OPDrms data are rescaled to a higher Mach number of 0.4, the SR data show an even more dramatic effect, see Figure 15. The hybrid flow control cases recovered the drop in Strehl Ratio related to the increase in the elevation angle, from as low as 0.53 and 0.14 at 148 degrees for M = 0.3 and M = 0.4 cases, respectively, up to an approximately constant value of 0.8 and 0.5, respectively, at all elevation angles. This result is very important for many practical applications, laser-based-communications, for instance, since it opens up a larger range of viewing angles without a big drop in the far-field laser intensity.

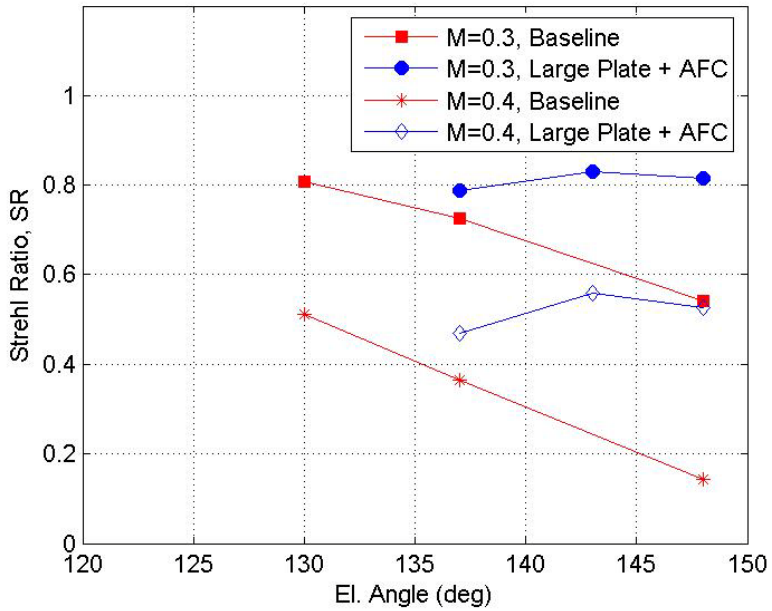

Figure 15. Far-Field Strehl Ratio for the turret for the baseline and the hybrid flow control

A point worth noting is that it is important to have the partition plate only upstream of the turret, but not downstream. Experiments with a hemisphere-on-surface[7] showed that despite the fact that the hemisphere is aerodynamically less protruding than the hemisphere-on-cylinder, aero-optically a hemisphere on a surface or plate is more aberrating than when it is elevated from the surface by a cylindrical base.[2]

The quality of 2-D WFS data, after significant post-processing, was found to be acceptable for most of the elevation angles. Also, 2-D WFS results were found to be quite consistent with results taken with the Malley probe in the previous studies of the optical studies around the turret[5]. Data from the distorted grating wavefront sensor after proper reduction were also found to be consistent with data from other sensors; however DGWFS wavefronts were found to be easily corrupted by the residual beam jitter on the laser beam and clipped-beam effects.

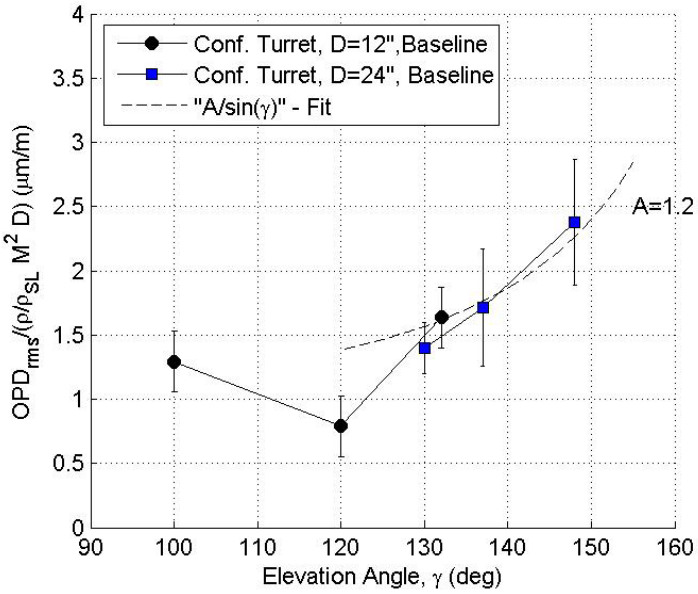

Figure 16. Normalized OPDrms for conformal-window turrets for different Reynolds numbers: D = 0.254 m, Re_D = 2.3x10^6 (from [3]) and the current study, baseline, D = 0.61 m, Re_D = 4.4x10^6.

In [2] it was proposed that for high enough Reynolds numbers and geometrically-similar turrets, the optical results do not depend on the Reynolds number and should scale as $OPD_{rms} = A \cdot (\rho / \rho_{SL}) M^2 D \cdot \frac{1}{\sin(\gamma)}$, where γ is the elevation angle and A is a function of the turret geometry. The non-dimensional results of the baseline measurements are plotted in Figure 16 as

a function of the elevation angle. Results of optical measurements on a smaller, but geometrically-similar turret are also plotted in Figure 16. They overlap quite well, further supporting both the supposition of [2] as well as the Reynolds-number independence. The constant, *A*, for this conformal-window turret was found to be 1.2. This important result allows us to apply the scaling to estimate optical aberrations for different turret sizes, elevation angles, and flight conditions.

Finally, the complexity of making aero-optical measurements in ever-larger wind tunnels cannot be over-staked. Even in wind tunnels specifically designed with aero-optic in mind, like the variety of tunnels at Notre Dame, making good aero-optical measurements is challenging; however, the largest tunnels founded at national facilities like Wright-Patterson AFB, and Arnold Engineering and Development Center were never envisioned as being used to make large-aperture wavefront measurements. Our experience indicates that contrary to common belief, optical environments posed by wind-tunnel facilities are worse than those found in flight. While the aero-optical and aerodynamic environments created by placing a turret either in a wind tunnel or on an airplane are essentially the same, the environment imposed by the tunnel and the aircraft are notably different. Since it is shared aero-optical environments that are of interest, it is important to continue to evolve our understanding of the non-shared tunnel conditions and how to deal with these in order to extract usable data. This paper described some of this evolving understanding. From this, the importance of using multiple (suite) of WFS types is again underscored. Also, it is clear that Zernike polynomials, so often used in treating optical systems, are better replaced when dealing with aero-optical phenomena. This paper demonstrates that POD, that is to say eigenmodes produced from the wavefront data itself, are more useful.

Acknowledgment

The authors would like to thank Kestrel Corporation, especially Paul Harrison and Boyd Hunter for collecting and partially reducing the DGWFS data. Also, we would like to thank the SARL personnel, especially Servane Altman for providing technical assistance during tests.

This work has been supported by the Boeing Company and Air Force Research Laboratory. The U.S. Government is authorized to reproduce and distribute reprints for governmental purposes notwithstanding any copyright notation therein.

References

[1]Gilbert, J. and Otten, L.J. (eds), *Aero-Optical Phenomena*, Progress in Astronautics and Aeronautics, Vol, **80**, AIAA, New York, 1982.

[2]S. Gordeyev and E. Jumper, “Fluid Dynamics and Aero-Optical Environment Around Turrets,” 40th AIAA Plasmadynamics and Lasers Conference, San-Antonio, TX, 22-25 June, 2009, AIAA Paper 2009-4224.

[3]S. Gordeyev, M. Post, T. MacLaughlin, J. Ceniceros and E. Jumper, "Aero-Optical Environment Around a Conformal-Window Turret", *AIAA Journal*, vol. **45**, No. 7, pp. 1514-1524, 2007.

[4]B. Vukasinovic, A. Glezer, S. Gordeyev, E. Jumper and V. Kibens "Fluidic Control of a Turret Wake, Part I: Aerodynamic Effects", 47th Aerospace Science Meeting and Exhibit, Orlando, Florida, 5-8 Jan, 2009, AIAA Paper 2009-0816.

[5]S. Gordeyev, E. Jumper, B. Vukasinovic, A. Glezer and V. Kibens, "Fluidic Control of a Turret Wake, Part II: Aero- Optical Effects", 47th Aerospace Science Meeting and Exhibit, Orlando, Florida, 5-8 Jan, 2009, AIAA Paper 2009-0817.

[6]Vukasinovic, B. and Glezer, A., "Control of a separating flow over a turret", AIAA Paper 2007-4506, 2007.

[7]Vukasinovic, B., Glezer, A., Gordeyev, S., Jumper, E., and Kibens, V., "Active control and optical diagnostics of the flow over a hemispherical turret, AIAA Paper 2009-598, 2008.

[8]B. Vukasinovic, A. Glezer, S. Gordeyev, E. Jumper and V. Kibens, "Hybrid Flow Control of a Turret Wake, Part I: Aerodynamic Effects ," 48th Aerospace Science Meeting and Exhibit, Orlando, Florida, 4-7 Jan, 2010, AIAA-2010-0086.

[9]Vukasinovic, B., Brzozowski, D., and Glezer, A., "Fluidic control of separation over a hemispherical turret", *AIAA J.*, Vol. **47**, No. 9, 2009, pp. 2212-2222.

[10]Smith, B.L. and Glezer, A.,"The Formation and Evolution of Synthetic Jets", *Phys. Fluids*, Vol. **10**, 1998, pp. 2281 – 2297.

[11]P. Blanchard, D. Fisher, S.C. Woods, and A.H. Greenaway, "Phase-Diversity Wave-Front Sensing With a Distorted Diffraction Grating," *Applied Optics* , Vol. **39**, No. 35, pp. 6649-6655.

[12]S.C. Woods and A.H. Greenaway," Wave-Front Sensing by Use of a Green's Function Solution to the Intensity Transport Equation," *J. Opt. Soc. Am. A*, Vol. **20**, No. 3, 2003, pp. 508-512.

[13]T. E. Gureyev, A. Roberts, K. A. Nugent, "Phase Retrieval With the Transport of Intensity Equation: Matrix Solution With Use of Zernike Polynomials", *JOSA*, Vol. **12**, No. 9, September 1995.

[14]R. A. Gonsalves, "Phase Retrieval and Diversity in Adaptive Optics", *Optical Engineering*, Vol. **21**, No. 5, September, October 1982.

[15]N. Baba, H. Tomita, N. Miura, "Iterative Reconstruction in Phase-Diversity Imaging", *Applied Optics*, Vol. **33**, No. 20, July 1994.

[16]Lumley J., *Stochastic Tools in Turbulence*, Academic Press, New York, 1970.

[17]Philip Holmes, John L. Lumley, and Gal Berkooz, *Turbulence, Coherent Structures, Dynamical Systems and Symmetry*, Cambridge University Press, 1998.